FORGE

Fate Of Repository Gases

European Commission FP7

MODELLING OF LAB AND FIELD EXPERIMENTS - HG-A EXPERIMENT

FORGE Report D 4.7 – VER 1.0

	Name	Organisation	Signature	Date
Compiled	François Bertrand, Frédéric Collin, Séverine Levasseur, Robert Charlier	University of Liege	François Bertrand, Frédéric Collin, Séverine Levasseur, Robert Charlier	5 August 2010
Verified	Robert Charlier	University of Liege	Robert Charlier	5 August 2010
Approved	Richard Shaw	BGS		1 September 2010

Euratom 7th Framework Programme Project: FORGE

EURATOM

Fate of repository gases (FORGE)

The multiple barrier concept is the cornerstone of all proposed schemes for underground disposal of radioactive wastes. The concept invokes a series of barriers, both engineered and natural, between the waste and the surface. Achieving this concept is the primary objective of all disposal programmes, from site appraisal and characterisation to repository design and construction. However, the performance of the repository as a whole (waste, buffer, engineering disturbed zone, host rock), and in particular its gas transport properties, are still poorly understood. Issues still to be adequately examined that relate to understanding basic processes include: dilational versus visco-capillary flow mechanisms; long-term integrity of seals, in particular gas flow along contacts; role of the EDZ as a conduit for preferential flow; laboratory to field up-scaling. Understanding gas generation and migration is thus vital in the quantitative assessment of repositories and is the focus of the research in this integrated, multi-disciplinary project. The FORGE project is a pan-European project with links to international radioactive waste management organisations, regulators and academia, specifically designed to tackle the key research issues associated with the generation and movement of repository gasses. Of particular importance are the long-term performance of bentonite buffers, plastic clays, indurated mudrocks and crystalline formations. Further experimental data are required to reduce uncertainty relating to the quantitative treatment of gas in performance assessment. FORGE will address these issues through a series of laboratory and field-scale experiments, including the development of new methods for up-scaling allowing the optimisation of concepts through detailed scenario analysis. The FORGE partners are committed to training and CPD through a broad portfolio of training opportunities and initiatives which form a significant part of the project.

Further details on the FORGE project and its outcomes can be accessed at www.FORGEproject.org.

FORGE –WP4

TASK 4.3 MODELLING OF LAB AND FIELD EXPERIMENTS

HG-A EXPERIMENT

Contacts

François Bertrand, Frédéric Collin, Séverine Levasseur, Robert Charlier

Université de Liège, Département ArGEnCo
Institut de Mécanique et de Génie Civil
Chemin des chevreuils, 1
4000 Liège

E-mail:
bertrand.francois@ulg.ac.be
f.collin@ulg.ac.be
severine.levasseur@ulg.ac.be
robert.charlier@ulg.ac.be

TABLE OF CONTENT

1. INTRODUCTION 3

2. MECHANICAL CONSTITUTIVE MODEL 4

3. HYDRAULIC CONSTITUTIVE MODEL 11

4. BALANCE EQUATIONS 12

5. MODEL PARAMETERS 13

6. SUBTASK 1. MODELLING OF TUNNEL EXCAVATION 14

7. REFERENCES 21

1. Introduction

The objective of the Hg-A experiment is to investigate the hydro-mechanical evolution of a backfilled and sealed tunnel section. In particular, the focus is made on the following aspects:
- the generation and the behaviour of Excavated Damaged Zone (EDZ)
- the upscaling of the hydraulic conductivity of Opalinus Clay from the lab test to the tunnel scale
- the investigation of self-sealing processes
- the estimation of gas leakage rates

The geometry of the problem consists in a tunnel of 13 m in length and 1.035 m in diameter drilled in Opalinus Clay. More than 20 observation boreholes have been drilled parallel and oblique to the microtunnel axis and equipped with multipacker piezometer systems, inclinometer chains, chain deflectometers and stress cells to monitor the correspondent parameters in the host rock (pore water pressure, total stress and displacements) (Figure 1). After excavation, the micro-tunnel has also been instrumented with surface extensometers, strain gages, time domain reflectometers (TDRs), piezometers and geophones.

The test plan consists in the drilling and instrumentation of the boreholes (Phase 0), the excavation of the microtunnel followed by backfilling and sealing (Phase 1), installation and inflation of the megapacker (Phase 2), hydraulic constant pressure and constant rate injection tests (Phase 3), gas injection tests (Phase 4) and a second hydraulic test series (Phase 5) (Trick et al., 2007) (Figure 2).

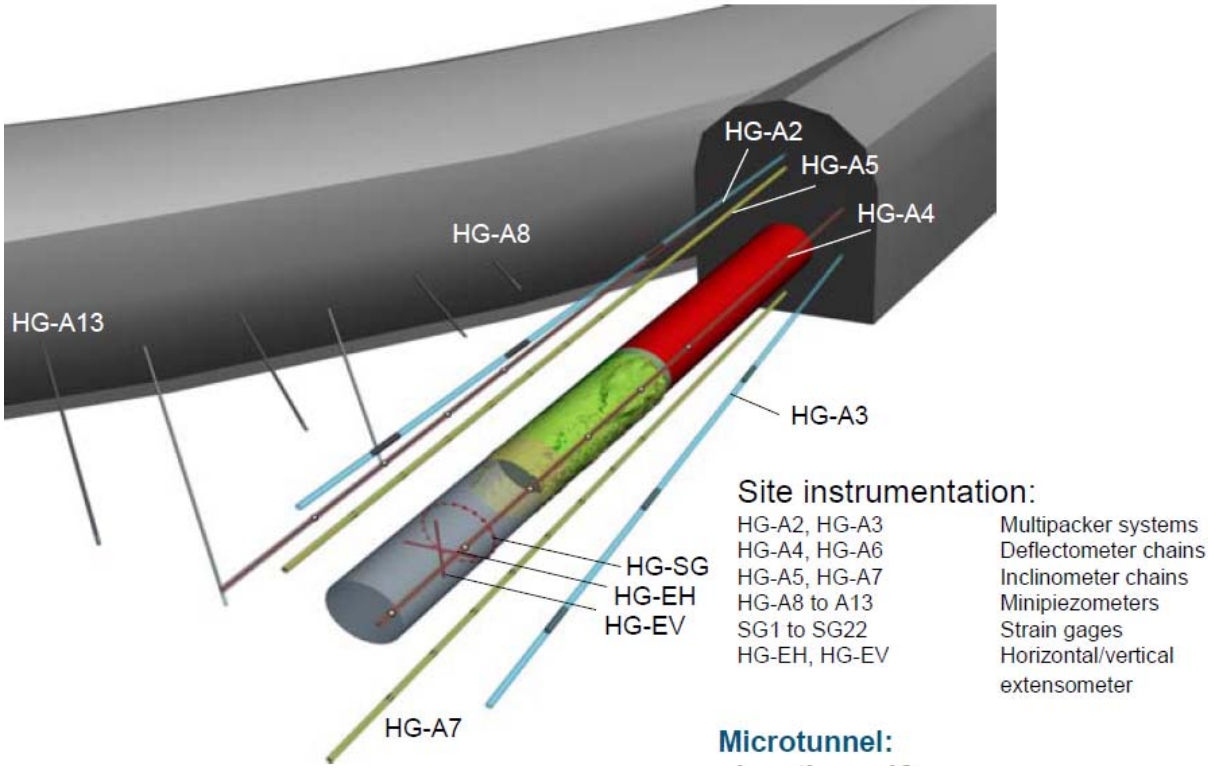

Figure 1: General layout of the Hg-A gallery with instrumentation boreholes (Trick et al., 2007)

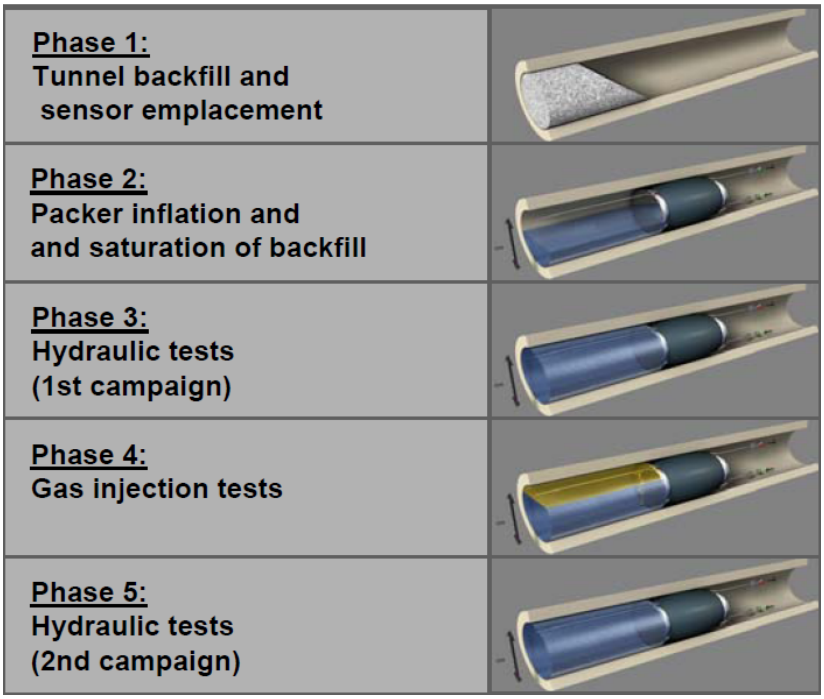

Figure 2: General test plan of the HG-A experiment (Trick et al., 2007)

In the framework of the Workpackage 4 (WP 4) – Task 4.3 (Modelling of lab and field experiments), the global approach of the phenomena are divided in four stage (I. Gaus, G.W. Lanyon, P. Marschall, J. Rueedi, 19 Nov. 2009, oral communication):

SubTask 1: *Modelling of tunnel excavation* considering mechanical behaviour of Opalinus Clay (including anisotropy and suction), development of EDZ.
SubTask 2: *Modelling of water injection* considering resaturation, evolution and role of EDZ, interpretation of long term injection tests and self-sealing.
SubTask 3*: Modelling of the gas injection* including the design and the prediction of gas injection phase, the model calibration, the test interpretation and the interpretation of the second set of hydrotests.
SubTask 4: *Insight modelling and upscaling*

2. Mechanical constitutive model

The model uses elastic cross-anisotropy coupled with an extended Drucker-Prager hardening plasticity model. The plastic yield limit considers that the material cohesion depends on the angle between major principal stress and the bedding orientation.

The elasto-plasticity principle (concept of a loading surface, f, in the stress space which limits the region of elastic deformation) allows that the total strain rate, $\dot{\varepsilon}_{ij}$, be split into elastic, $\dot{\varepsilon}_{ij}^{e}$, and plastic, $\dot{\varepsilon}_{ij}^{p}$, components :

$$\dot{\varepsilon}_{ij} = \dot{\varepsilon}_{ij}^{e} + \dot{\varepsilon}_{ij}^{p} \qquad (1)$$

Because of elastic anisotropy, the elasto-plastic stress-strain relations are more convenient to be expressed in the anisotropic axis, as indicated by the star in exponent (σ'^{*}_{ij} and ε^{*}_{ij})

$$\dot{\sigma}'^{*}_{ij} = C_{ijkl}\dot{\varepsilon}^{*}_{kl} \tag{2}$$

where C_{ijkl} is the elasto-plastic constitutive matrix.

In the more general situation, the reference axes do not coincide with the axes of anisotropy and the expression of σ'^{*}_{ij} and ε^{*}_{ij} can be obtained from σ'_{ij} and ε_{ij} expressed in the system of reference through the following transformation:

$$\sigma'^{*}_{ij} = R_{ki}R_{lj}\sigma'_{kl} \quad ; \quad \varepsilon^{*}_{ij} = R_{ki}R_{lj}\varepsilon_{kl} \tag{3}$$

where R_{ij} is the ij component of the rotation matrix:

$$R = \begin{bmatrix} \cos\alpha\cos\varphi & \sin\alpha\cos\varphi & \sin\varphi \\ -\sin\alpha\cos\theta - \sin\theta\sin\varphi\cos\alpha & \cos\alpha\cos\theta - \sin\theta\sin\varphi\sin\alpha & \sin\theta\cos\varphi \\ \sin\theta\sin\alpha - \cos\alpha\sin\varphi\cos\theta & -\sin\varphi\sin\alpha\cos\theta - \sin\theta\cos\alpha & \cos\varphi\cos\theta \end{bmatrix} \tag{4}$$

where α is the rotation angle around the axes $\underline{E}_3$ (rotation in the $(\underline{E}_1, \underline{E}_2)$) plane, the angles φ and θ defines the rotation around the axes $\underline{e}'_2$ and $\underline{e}_1$, respectively (Figure 3). The positive direction of rotation is counter-clockwise. $(\underline{E}_1, \underline{E}_2, \underline{E}_3)$ and $(\underline{e}_1, \underline{e}_2, \underline{e}_3)$ are the reference axes and the anisotropic axes, respectively.

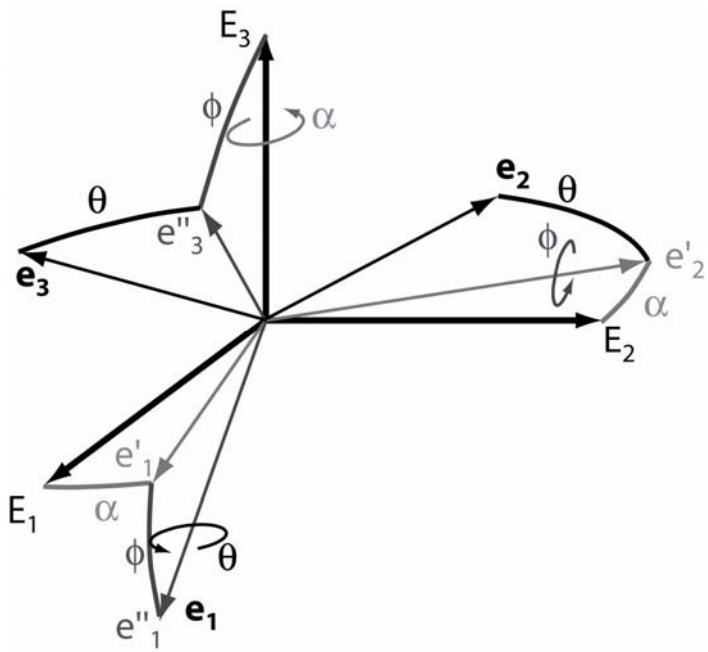

Figure 3: Transformation of the global axis $(\underline{E}_1, \underline{E}_2, \underline{E}_3)$ into anisotropic axes $(\underline{e}_1, \underline{e}_2, \underline{e}_3)$.

At the end of each step of computation, the stress and strain obtained in the anisotropic axes (σ'^{*}_{ij} and ε^{*}_{ij}) are re-transformed to be expressed in the global axes (σ'_{ij} and ε_{ij}):

$$\sigma'_{ij} = R_{ik} R_{jl} \sigma'^{*}_{kl} \quad ; \quad \varepsilon_{ij} = R_{ik} R_{jl} \varepsilon^{*}_{kl} \tag{5}$$

Elastic anisotropy

$\dot{\varepsilon}^{*e}_{ij}$ is the ij strain rate component that does not modify the hardening state of the material. $\dot{\varepsilon}^{*e}_{ij}$ is linked to stress rate through the Hooke law :

$$\dot{\varepsilon}^{*e}_{ij} = D^{e}_{ijkl} \dot{\sigma}'^{*}_{kl} \tag{6}$$

The D^{e}_{ijkl} matrix considers anisotropic elasticity. Considering the requirement of symmetry of the stiffness matrix, the anisotropic elasticity needs a maximum of 21 independent parameters to be fully described. However, axes of symmetry in the structure of many materials limit the number of independent parameters. An anisotropy induced by three orthogonal structural directions, usually called *orthotropy,* requires 9 parameters to define the elastic matrix, as follow:

$$D^{e}_{ijkl} = \begin{bmatrix} \frac{1}{E_1} & -\frac{\nu_{21}}{E_2} & -\frac{\nu_{31}}{E_3} & & & \\ -\frac{\nu_{12}}{E_1} & \frac{1}{E_2} & -\frac{\nu_{32}}{E_3} & & & \\ -\frac{\nu_{13}}{E_1} & -\frac{\nu_{23}}{E_2} & \frac{1}{E_3} & & & \\ & & & \frac{1}{2G_{12}} & & \\ & & & & \frac{1}{2G_{13}} & \\ & & & & & \frac{1}{2G_{23}} \end{bmatrix} \tag{7}$$

The symmetry of the stiffness matrix imposes that

$$\frac{\nu_{21}}{E_2} = \frac{\nu_{12}}{E_1} \quad ; \quad \frac{\nu_{31}}{E_3} = \frac{\nu_{13}}{E_1} \quad ; \quad \frac{\nu_{23}}{E_2} = \frac{\nu_{32}}{E_3} \tag{8}$$

By inversing the matrix D^{e}_{ijkl}, the elastic relation is:

$$\dot{\sigma}'^{*}_{ij} = C^{e}_{ijkl} \dot{\varepsilon}^{*e}_{kl} \tag{9}$$

with

$$C^{e}_{ijkl} = \begin{bmatrix} \frac{1-\nu_{23}\nu_{32}}{E_2E_3\det} & \frac{\nu_{21}+\nu_{31}\nu_{23}}{E_2E_3\det} & \frac{\nu_{21}\nu_{32}+\nu_{31}}{E_2E_3\det} & & & \\ \frac{\nu_{12}+\nu_{13}\nu_{32}}{E_1E_3\det} & \frac{1-\nu_{13}\nu_{31}}{E_1E_3\det} & \frac{\nu_{32}+\nu_{31}\nu_{12}}{E_1E_3\det} & & & \\ \frac{\nu_{13}+\nu_{23}\nu_{12}}{E_1E_2\det} & \frac{\nu_{23}+\nu_{21}\nu_{13}}{E_1E_2\det} & \frac{1-\nu_{21}\nu_{12}}{E_1E_2\det} & & & \\ & & & 2G_{12} & & \\ & & & & 2G_{13} & \\ & & & & & 2G_{23} \end{bmatrix} \tag{10}$$

with

$$\det = \frac{1-\nu_{31}\nu_{13}-\nu_{21}\nu_{12}-\nu_{32}\nu_{23}-2\nu_{31}\nu_{12}\nu_{23}}{E_1E_2E_3} \tag{11}$$

Sedimentary rocks show usually a more limited form of anisotropy. The behaviour is isotropic in the plane of bedding and the unique direction of anisotropy is perpendicular to bedding. The properties of such materials are independent of rotation about an axis of symmetry normal to the bedding plane (Graham and Houlsby, 1982). This type of elastic anisotropy, called *transverse isotropy* or *cross-anisotropy*, requires 5 independent parameters and is a particular case of Equations (7) and (10) for which

$$\begin{cases} E_1 = E_2 = E_{//} \\ E_3 = E_{\perp} \\ \nu_{12} = \nu_{//,//} \\ \nu_{13} = \nu_{23} = \nu_{//,\perp} \\ G_{13} = G_{23} = G_{//,\perp} \\ G_{12} = G_{//,//} = \dfrac{E_{//}}{2\left(1+\nu_{//,//}\right)} \end{cases} \tag{12}$$

where the subscripts // and $\perp$ indicates, respectively, the direction parallel to bedding (directions 1 and 2) and perpendicular to bedding (direction 3).

Plasticity

The Drucker-Prager plastic yield limit, flow rule and consistency condition are expressed in the anisotropic axis (stress and strain components are expressed with a star exponent). This way of proceed aims at keeping the elastic matrix (needed in the development of the consistency condition) as simple as possible.

The limit between the elastic and the plastic domain is represented by a yield surface in the principal stress space. This surface corresponds to the Drucker-Prager yield surface f (Drucker and Prager, 1952):

$$f = II_{\hat{\sigma}} - m\left(I_{\sigma} - \frac{3c}{\tan\phi} \right) = 0 \tag{13}$$

with

$$m = \frac{2\sin\phi}{\sqrt{3}\left(3 - \sin\phi\right)} \tag{14}$$

I_{σ} and $II_{\hat{\sigma}}$ are the first stress tensor invariant and the second deviatoric stress tensor invariant, respectively:

$$I_{\sigma} = \sigma'^{*}_{ii} \tag{15}$$

$$II_{\hat{\sigma}} = \sqrt{\frac{1}{2}\hat{\sigma}'^{*}_{ij}\hat{\sigma}'^{*}_{ij}} \quad ; \quad \hat{\sigma}'^{*}_{ij} = \sigma'^{*}_{ij} - \frac{I_{\sigma}}{3}\delta_{ij} \tag{16}$$

In Equation (13), the linear coefficient m between the first and the second stress invariant being independent of the third invariant (or alternatively, the Lode angle), the plastic surface is a cone in the principal stress space. The trace of this plasticity surface on the Π plane (deviatoric plane) is a circle (Figure 4).

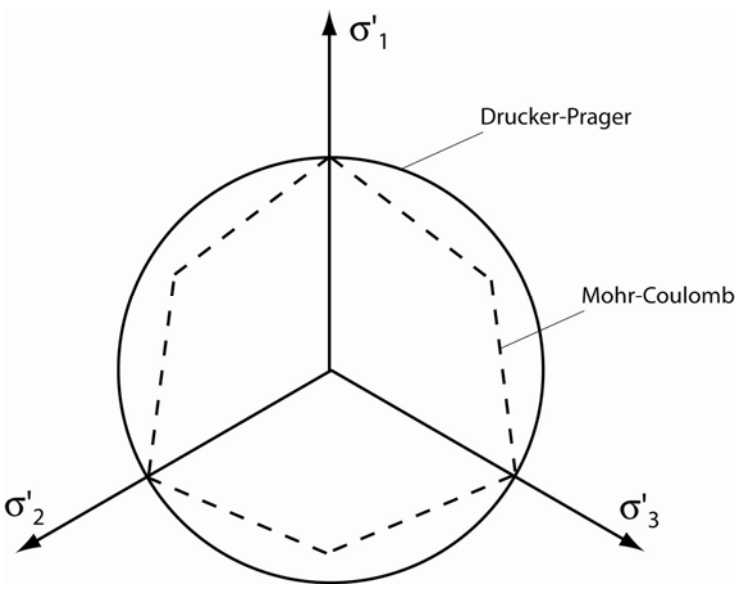

Figure 4: Yield surface of the Drucker-Prager criterion in the deviatoric plane. Comparison with the Mohr-Coulomb yield surface.

The material cohesion depends on the angle between major principal stress and the normal to the bedding plane. Three cohesion values are defined, for major principal stress parallel ($\alpha_{\sigma_1} = 0°$), perpendicular ($\alpha_{\sigma_1} = 90°$) and with an angle of 45° ($\alpha_{\sigma_1} = 45°$) with respect to the normal to bedding plane. Between those values, cohesion varies linearly with α_{σ_1}. The mathematical expression of the cohesion is as follows (Figure 5):

$$c = \max\left[\left(\frac{c_{45°} - c_{0°}}{45°}\right)\alpha_{\sigma_1} + c_{0°}\ ;\ \left(\frac{c_{45°} - c_{0°}}{45°}\right)\left(\alpha_{\sigma_1} - 45°\right) + c_{45°}\right] \tag{17}$$

with α_{σ_1} being the angle between the normal to the bedding plane $\vec{n}$ and the major principal stress $\vec{\sigma}_1$:

$$\alpha_{\sigma_1} = \arccos\left(\frac{\vec{n}.\vec{\sigma}_1'}{\|\vec{n}\|\|\vec{\sigma}_1'\|}\right) \tag{18}$$

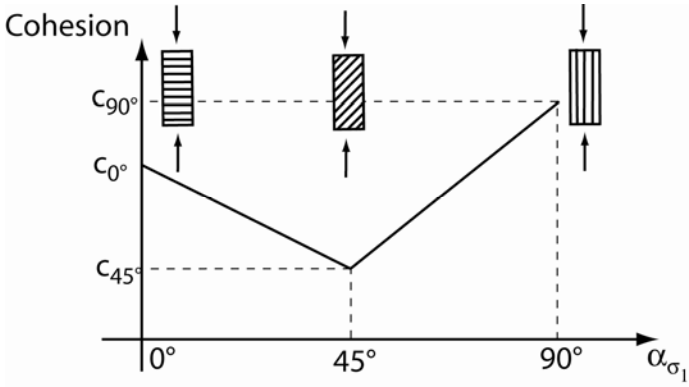

Figure 5: Schematic view of the cohesion evolution as a function of the angle between the normal vector to bedding plane and the direction of major principal stress.

A general non-associated plasticity framework is considered:

$$\dot{\varepsilon}_{ij}^{*p} = \lambda^P \frac{\partial g}{\partial \sigma_{ij}'^*} \tag{19}$$

with the plastic potential g defined as:

$$g = II_{\hat{\sigma}} + m' I_\sigma = 0 \tag{20}$$

with

$$m' = \frac{2\sin\psi}{\sqrt{3}\left(3 - \sin\psi\right)} \tag{21}$$

where ψ is the dilatancy angle. When $\psi = \phi$, $\frac{\partial f}{\partial \sigma_{ij}'^*} = \frac{\partial g}{\partial \sigma_{ij}'^*}$ and the flow rule is associated.

The plastic multiplier λ^p is obtained from the consistency condition which states that during plastic flow, the stress state stays on the limit surface:

$$df = \frac{\partial f}{\partial \sigma_{ij}'^*}\dot{\sigma}_{ij}'^* + \frac{\partial f}{\partial \kappa}\dot{\kappa} = 0 \tag{22}$$

with κ being the hardening variable(s). The used model is a hardening Drucker-Prager model that allows hardening/softening processes during plastic flow. This is introduced via an hyperbolic variation of the friction angle and the cohesion between initial (ϕ_0 and c_0) and final (ϕ_f and c_f) values as a function of the Von Mises equivalent plastic strain ε_{eq}^p (Barnichon, 1998):

$$\phi = \phi_0 + \frac{\left(\phi_f - \phi_0\right)\varepsilon_{eq}^p}{B_p + \varepsilon_{eq}^p} \tag{23}$$

$$c = c_0 + \frac{\left(c_f - c_0\right)\varepsilon_{eq}^p}{B_c + \varepsilon_{eq}^p} \tag{24}$$

where the Von Mises equivalent plastic strain ε_{eq}^p is obtained by integration of the Von Mises equivalent plastic strain rate $\dot{\varepsilon}_{eq}^p$:

$$\varepsilon_{eq}^p = \int_0^t \dot{\varepsilon}_{eq}^p dt \quad ; \quad \dot{\varepsilon}_{eq}^p = \sqrt{\frac{2}{3}\dot{\hat{\varepsilon}}_{ij}^{*p}\dot{\hat{\varepsilon}}_{ij}^{*p}} \tag{25}$$

Coefficients B_p and B_c represent respectively the values of equivalent plastic strain for which half of the hardening/softening on friction angle and cohesion is achieved (Figure 6).

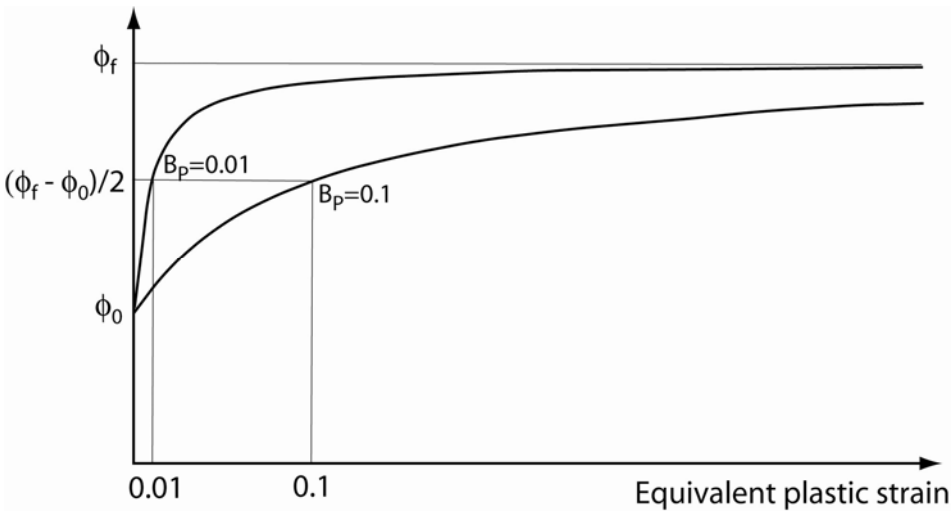

Figure 6: Hardening/softening hyperbolic relation for 2 values of coefficient Bp

Thus, the consistency condition (Equation 22) reads:

$$df = \frac{\partial f}{\partial \sigma_{ij}'^*}\dot{\sigma}_{ij}'^* + \left(\frac{\partial f}{\partial \phi}\frac{d\phi}{d\varepsilon_{eq}^p} + \frac{\partial f}{\partial c}\frac{dc}{d\varepsilon_{eq}^p}\right)\dot{\varepsilon}_{eq}^p = 0 \tag{26}$$

The Von Mises equivalent plastic strain can be expressed as a function of the plastic multiplier combining Equations (19) and (25), for the specific expression of the Drucker-Prager plastic potential (20):

$$\dot{\varepsilon}_{eq}^{p} = \sqrt{\frac{2}{3}\left(\frac{\partial g}{\partial \sigma_{ij}'^{*}}\frac{\partial g}{\partial \sigma_{ij}'^{*}} - \frac{1}{3}\frac{\partial g}{\partial \sigma_{kk}'^{*}}\frac{\partial g}{\partial \sigma_{ll}'^{*}}\right)}\lambda^{P} = \frac{\sqrt{3}}{3}\lambda^{P} \tag{27}$$

Combining together the elastic relation (9) and expression of plastic strain (19) gives:

$$\dot{\sigma}_{ij}^{*} = C_{ijkl}\left(\dot{\varepsilon}_{kl}^{*} - \lambda^{p}\frac{\partial g}{\partial \sigma_{kl}'^{*}}\right) \tag{28}$$

That allows us to determine the plastic multiplier λ^{p}:

$$\lambda^{p} = \frac{\frac{\partial f}{\partial \sigma_{ij}'^{*}} C_{ijkl}^{e}\dot{\varepsilon}_{kl}^{*}}{\frac{\partial f}{\partial \sigma_{mn}'^{*}} C_{mnop}^{e} - \frac{\sqrt{3}}{3}\left(\frac{\partial f}{\partial \phi}\frac{d\phi}{d\varepsilon_{eq}^{p}} + \frac{\partial f}{\partial c}\frac{dc}{d\varepsilon_{eq}^{p}}\right)} \tag{29}$$

3. Hydraulic constitutive model

Darcy's law

The general Darcy flow law is used and defines the Darcy fluid velocity $\underline{q}_{w}$ as a linear function of permeability and the gradient of fluid pressure p_{w} :

$$\underline{q}_{w} = -\underline{k}\left(\nabla p_{w}\right) \tag{30}$$

The permeability tensor $\underline{k}$ depends on the degree of saturation of the material:

$$\underline{k} = k_{r}\ \underline{k}_{sat} \tag{31}$$

with k_{r} being the relative permeability coefficient as defined by Marschall et al. (2005) for the Opalinus Clay:

$$k_{rw} = \sqrt{S_{r}}\left(1-(1-S_{r}^{2})^{0.5}\right)^{2} \tag{32}$$

where S_{r} is the degree of saturation.

In order to consider anisotropic permeability, $\underline{k}$ is a tensor.

Retention curve

The degree of saturation is related to suction by the following expression:

$$S_r = \left(1 + \left(\frac{-p_w}{CSR1}\right)^{CSR2}\right)^{-(1-\frac{1}{CSR2})} \tag{33}$$

where CSR1 and CSR2 are material parameters.

Water specific mass

The water specific mass depends on pore water pressure :

$$\rho_w = \rho_{w0}\left[1 + \frac{p_w - p_{w0}}{\chi_w}\right] \tag{34}$$

where ρ_{w0} is the reference water specific mass at reference pore water pressure χ_w is the liquid compressibility coefficient.

4. Balance equations

Momentum balance equation

The momentum balance equation is written for quasi-static conditions:

$$div(\sigma_{ij}) = 0 \tag{35}$$

where σ_{ij} is the total stress tensor [Pa]

The total stress is expressed by:

$$\sigma_{ij} = \sigma'_{ij} - b\ S_r\ p_w \tag{36}$$

where b is the Biot coefficient and σ'_{ij} the effective stress.

Water mass balance equation

We suppose that the water is only in its liquid phase. Then, the water mass balance equation can be written:

$$\frac{\partial}{\partial t}\left(\rho_w n S_r\right) + div\left(\rho_w\ \underline{q}_w\right) = Q_w \tag{37}$$

where $\underline{q}_w$ is the mean speed of the liquid phase compared to the solid phase [m.s-1] and ρ_w is the bulk density of water [kg.m-3].

5. Model parameters

The geomechanical characteristics, as presented in Table 1 have been determined through the comparison between experimental results and numerical modelling of triaxial tests with three different inclinations of the bedding plane with respect to the loading direction (α_{σ_1} =0°, 45° and 90°): bedding planes parallel (P-Sample, α_{σ_1} = 90°), perpendicular (S-Sample, α_{σ_1} = 0°) and with an inclination of 45°C (Z-Sample, α_{σ_1} = 45°) with respect to the loading direction (Figure 7). The elastic stiffness and the shear strength are clearly affected by the direction of loading with respect to the bedding plane. The elastic rigidity of the Z-sample is included between the rigidity of P- and S- samples which is characteristics of cross-anisotropic behaviour. The comparison between experimental results (compiled by Laloui and François 2008) and numerical simulations is made in Figure 8.

The hydraulic parameters have been obtained from the literature (Gens et al., 2007, Wileveau 2005, Martin and Lanyon 2003).

Geomechanical characteristics			
Young elastic modulus	[GPa]	$E_{//}$	16
Young elastic modulus	[GPa]	$E_{\perp}$	3
Poisson ratio	[-]	$\upsilon_{////}$	0.27
	[-]	$\upsilon_{//\perp}$	0.27
		$c_{0,0°}$	4.2 (0°)
Initial cohesion	[MPa]	$c_{0,45°}$	0.7 (45°)
		$c_{0,90°}$	7 (90°)
		$c_{f,0°}$	6 (0°)
Final cohesion	[MPa]	$c_{f,45°}$	3 (45°)
		$c_{f,90°}$	10 (90°)
Softening parameter	[-]	B_c	0.01
Initial friction angle	[°]	$\varnothing_{c0}$	14
Final friction angle	[°]	$\varnothing_{cf}$	20
Hardening parameter	[-]	B_{ϕ}	0.01
Dilatation angle	[°]	Ψ	0
Biot's coefficient	[-]	b	0.6

Table 1 : Geomechanical characteristics

Hydraulic characteristics			
Initial porosity	[-]	n_0	0.1
Initial intrinsic permeability	[m/s]	$k_{sat,//}$	4.10^{-13}
		$k_{sat,\perp}$	4.10^{-14}
Water specific mass	[kg/m³]	ρ_w	1000
Fluid dynamic viscosity	[Pa.s]	μ_w	10^{-3}
Liquid compressibility coefficient	[MPa^{-1}]	$1/\chi_w$	5.10^{-4}
Coefficient of the water retention curve	[MPa]	CSR1	5
	[-]	CSR2	1.2

Table 2: Hydraulic characteristics

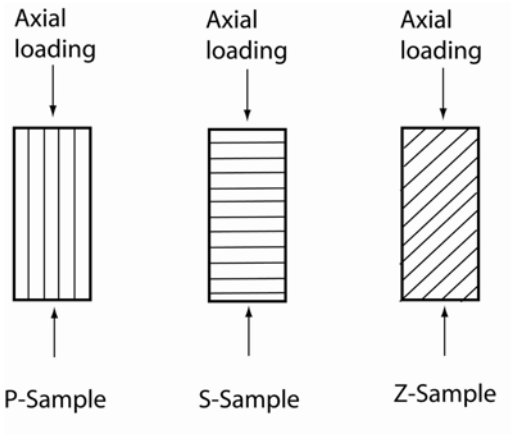

Figure 7: Orientation of bedding with respect to the loading direction in P-, S- and Z- samples

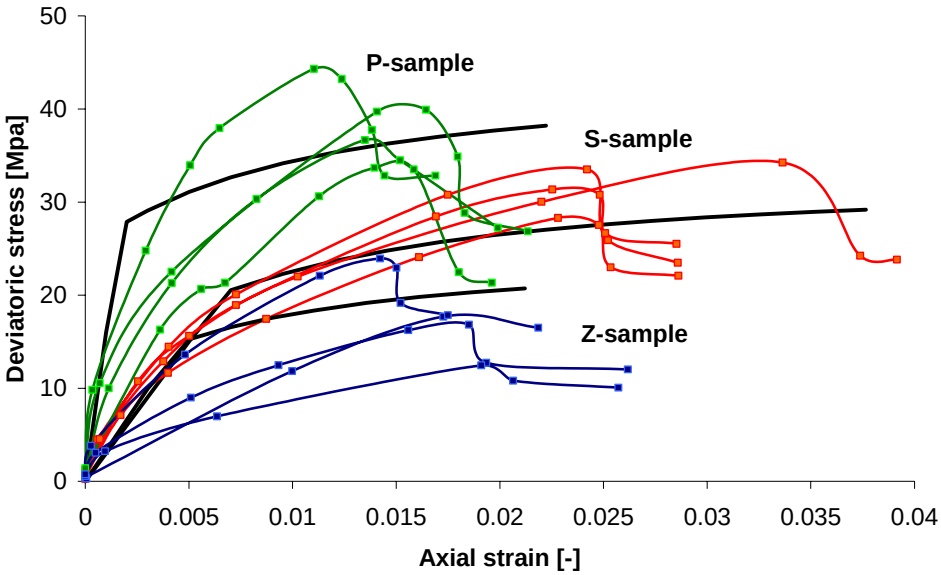

Figure 8: Comparison between numerical simulations and experimental results of triaxial compression tests with a confining pressure of 15 MPa and three different orientation of bedding with respect to axial loading.

6. SubTask 1. Modelling of tunnel excavation

Based on the in-situ measurements, the objective of the modelling of the excavation phase is to identify the concepts, the processes and the parameters of models in order to reproduce the creation and evolution of the EDZ. Also, those modelling will indicate the accuracy and the relevance of current models to predict EDZ structure.

Geometry and boundary conditions

The Hg-A gallery has been excavated from a niche of the Gallery 04 of the Mont-Terri laboratory. The drilling is parallel to the bedding orientation. In a section perpendicular to the gallery, the bedding plane is oriented at 45° with respect to horizontal direction (Figure 9).

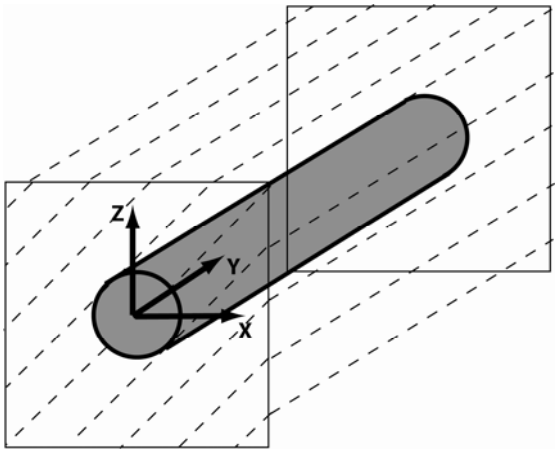

Figure 9: Schematic view of the orientation of the Hg-A gallery with respect to bedding plane.

The problem has been considered as a 2D plane strain problem, considering a perpendicular section in the middle of the gallery. A 40 m wide square domain has been considered. The initial stress is anisotropic: σ_Z = 8 MPa (vertical stress), σ_X = 3 MPa (horizontal radial stress) and σ_Y = 1.3 MPa (horizontal axial stress). The initial pore water pressure has been fixed to 0.9 MPa.

In term of mechanical conditions, the external boundaries are kinematically constrained (no displacement) (Figure 10). The internal boundary (at the gallery wall) is stress controlled. To simulate the excavation phase, the total stress at the gallery wall is decreased from the initial anisotropic stress to 0 MPa within one day (86400 s). The pore water pressure is maintained constant at 0.9 MPa on the external boundaries while the pore water pressure at the gallery wall is reduced from 0.9 MPa to 0 MPa in 1 day. Afterward, to reproduce gallery ventilation, pore water pressure is linearly decreased from 0 to -24 MPa in 7 days and then a constant pressure of -24 MPa is maintained. Seepage elements are considered on the gallery wall. That condition allows flow of water from the ground to the gallery (if the pore pressure of the ground is higher than the imposed pore pressure at the gallery wall) but restrict flow of water from the gallery to the ground.

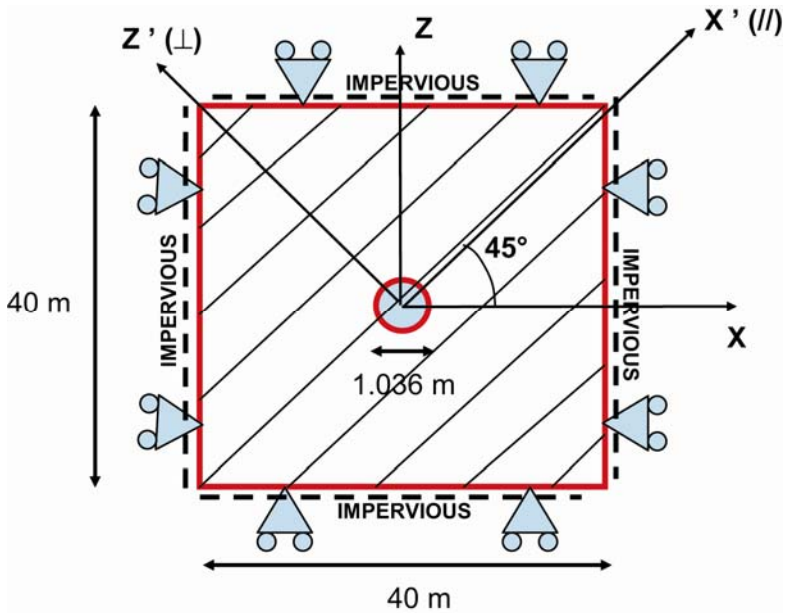

Figure 10: Boundary conditions of the 2D plane strain model.

Numerical results

The hydro-mechanical response of Opalinus Clay around the excavated gallery has been simulated over a period of 322 days (from 18th February to 31st December 2005). The numerical results are compared with in-situ measurements in sensor Hg-A2 and Hg-A3 for pore water pressure and Hg-A5 and Hg-A7 for displacements. The locations of the sensors are reported in Figure 11.

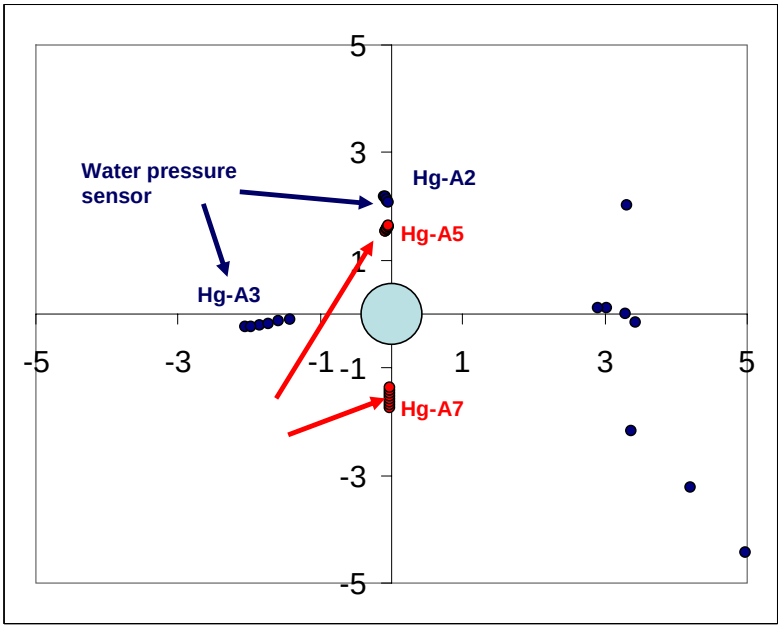

Figure 11: Projection of the sensor location in the 2D modelling section.

Figure 12 shows the rapid increase of pore water pressure in sensor Hg-A3 while sensors Hg-A2 measures a slight increase of pore water pressure. This difference in the pore water pressure response according to the radial direction of observation is due to the different sources of anisotropy (elastic, plastic, hydraulic and stress state). The main contribution of this difference is probably the anisotropy of the stress state. Vertical stress being much higher than horizontal stress, the gallery wall displacement is higher in the vertical direction, inducing a dilatation of pore space along with a decrease of pore water pressure (sensor Hg-A2). On the contrary, in the horizontal direction (sensor Hg-A3), the behaviour is more compressive, inducing drastic increase of the pore water pressure.

The numerical simulation is able to reproduce the main trends of pore water pressure evolutions. However, from a quantitative point of view, the comparisons show some discrepencies between numerical and experimental results:

- The intensity of the peak of the pore water pressure evolution measured by sensor Hg-A3 is underestimated by the numerical simulations.
- The pore water pressure decrease, after the peak is faster in the numerical simulations.
- The experimental measurement of the pore water pressure in sensor Hg-A2 shows a slight increase of pore water pressure until 50 days after excavation while the numerical modelling predicts an immediate decrease of the pore water pressure.

Figure 13 compares total displacement of sensor Hg-A5 (1m above the gallery) and Hg-A7 (1m below the excavation). After an immediate displacement 0.5 mm, the displacements continue to increase due to consolidation processes. The immediate response is well reproduced by the model. However, the subsequent evolution of the displacements is slightly under-estimated by the model. The modelled displacement in sensor Hg-A5 and Hg-A7 are equal but opposite in sign. This is because those sensors are located in symmetric orientations (-90° and +90°) with respect to the different anisotropic directions: 45° and 135° for elastic modulus, cohesion and water permeability and 0° and 90° for in-situ stress.

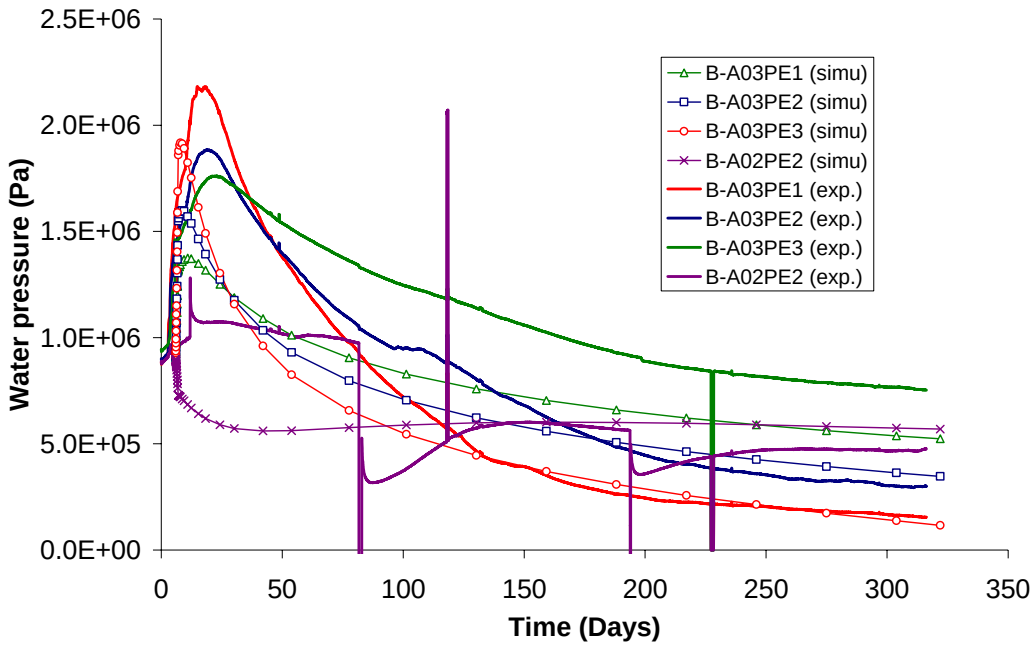

Figure 12: Comparison between numerical simulation and experimental results of the time evolution of the pore water pressure in sensor Hg-A02 and Hg-A03.

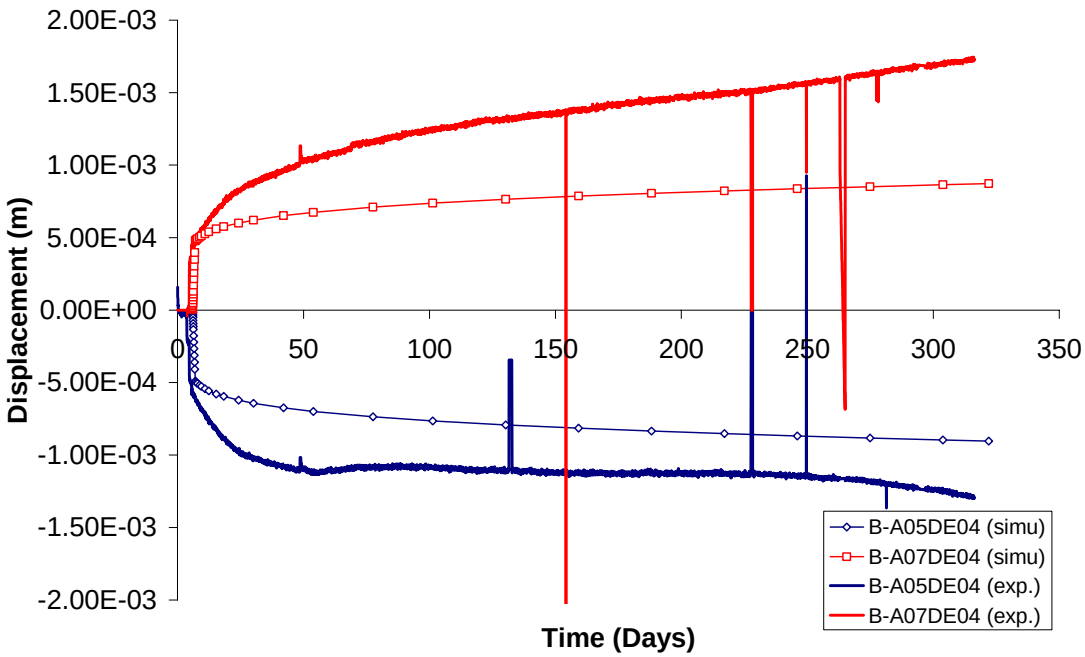

Figure 13: Comparison between numerical simulation and experimental results of the time evolution of the total displacement in sensor Hg-A05 and Hg-A07.

Even if the general trend of numerical results is in good agreement with experimental measurements, the quantitative differences can be related to two aspects:

- The model parameters of the mechanical model have been determined from independent triaxial tests. So, the numerical simulations consist in blind prediction and not in an optimization procedure.
- The 3D complex geometry of the system has been simplified into a 2D plane strain problem. The effect of the impervious liner installed in the 6 first meters of the gallery has not been considered. However, this liner has a mechanical and hydraulic effect on the global hydro-mechanical response. Also, the 2D simulation does not allow the consideration of the excavation step. Finally, all the sensors that are located in a 3D space have been projected in the 2D modelled plane. So, the longitudinal location of the sensors has not been considered in the simulation.

Result interpretations

Because of the difference sources of anisotropy, the hydro-mechanical response of Opalinus clay around the excavated gallery is not axisymmetric. The anisotropic stress state tends to induce two distinct behaviours on vertical and horizontal directions: an extensional behaviour (negative variation of pore water pressure) in the vertical direction and a compressive behaviour (positive variation of pore water pressure) in the horizontal direction. On the contrary, elastic anisotropy provokes higher variation of pore pressure in the stiffer direction (parallel to bedding) and less variation of pore pressure (or even negative variation) in the less rigid direction (perpendicular to bedding). Finally, anisotropic permeability makes drainage faster in the direction parallel to bedding. So, the combination of all sources of anisotropy makes complex the pore water pressure evolution. Figure 14 and 15 shows the pore water pressure distribution at day 0 (immediately after excavation) and day 316, respectively. After one year of ventilation of the gallery, the negative pore water pressure propagates faster in the more permeable direction (parallel to bedding).

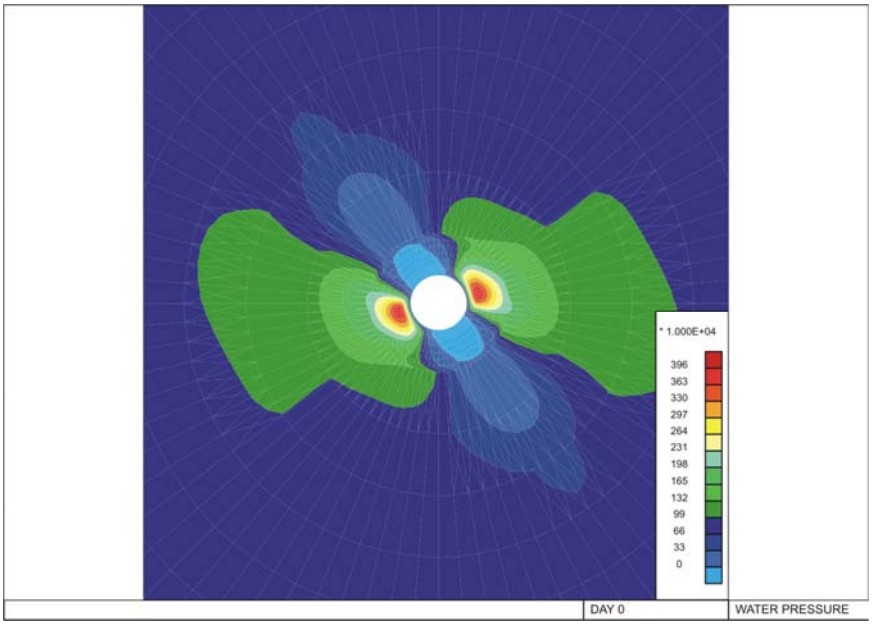

Figure 14: Numerical prediction of the pore water pressure distribution around the gallery at day 0 (just after excavation)

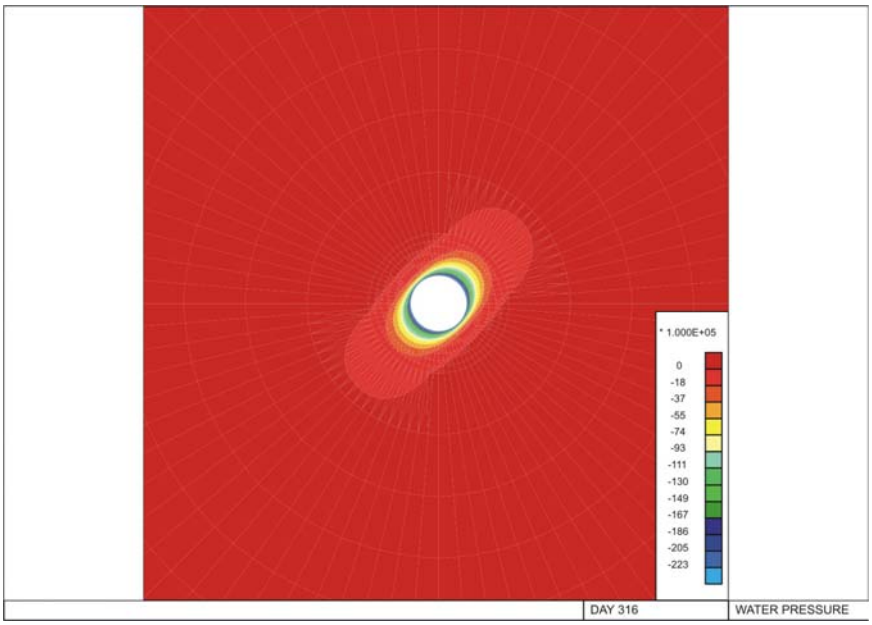

Figure 15: Numerical prediction of the pore water pressure distribution around the gallery at day 316 (after almost one year of ventilation)

Figure 16 shows the deformed mesh one year after the excavation. The minimum and maximum displacements occur at 30° and 120° with respect to x axis, respectively.

At short term after excavation, plastic zone develops in preferential directions at 30° and 150° with respect to x-axis (Figure 17). Those directions correspond probably to the zone in which maximum shear stresses are concentrated. At the end of the simulation, the negative pore water pressure (suction) induced by the gallery ventilation provokes an increase in strength. As a consequence, the plastic processes are suppressed and the behaviour is elastic (Figure 18).

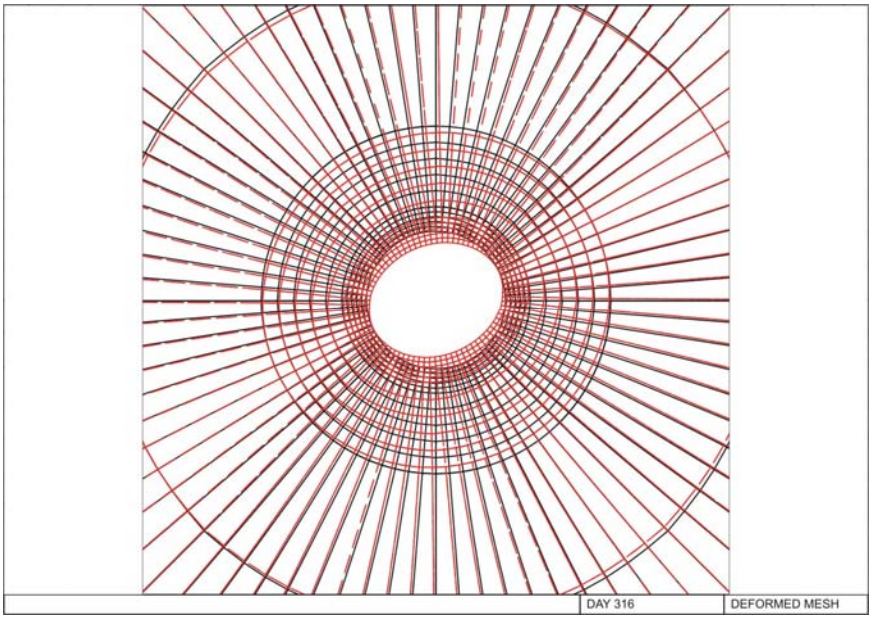

Figure 16: Numerical prediction of the deformation of the gallery at day 316 (after almost one year of ventilation). Maximum displacement: 2.05mm.

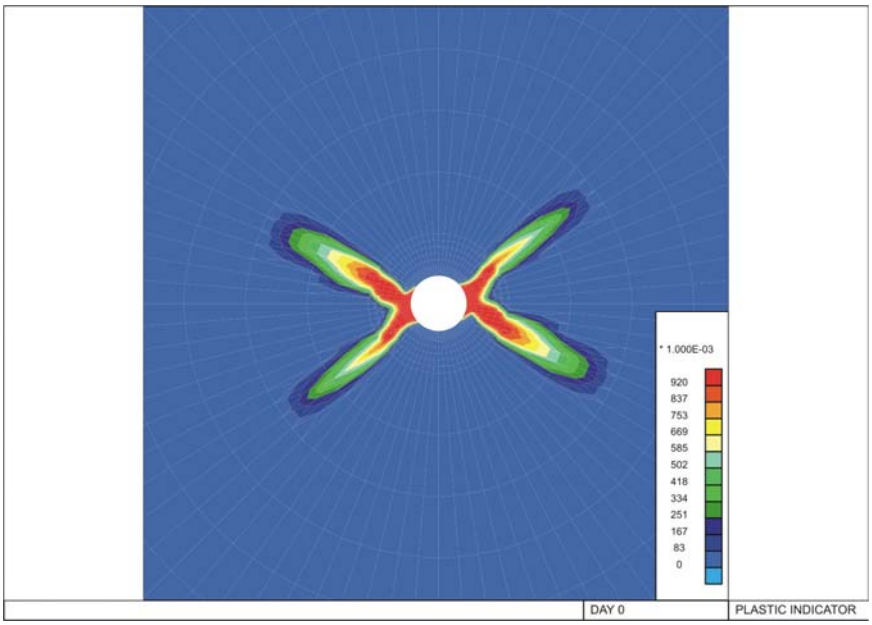

Figure 17: Numerical prediction of the plastic zone at day 0 (just after excavation). Red: Active plastic zone; Other colors: non-active plastic zone.

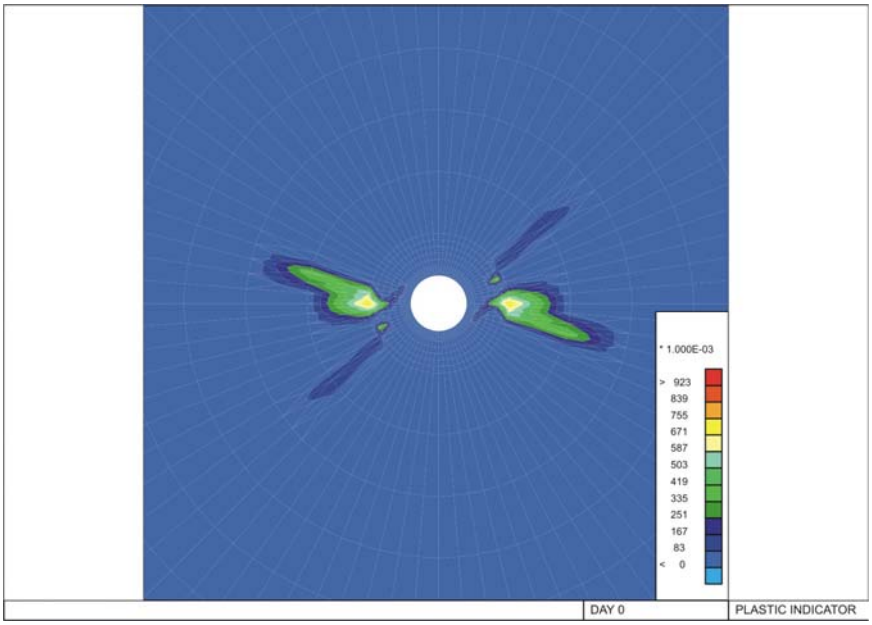

Figure 18: Numerical prediction of the plastic zone at day 316 (after almost one year of ventilation). Red: Active plastic zone; Other colors: non-active plastic zone.

Conclusions

The hydro-mechanical behaviour of Opalinus Clay around a excavated gallery has been numerically simulated. Numerical results have been compared with available in-situ experimental measurements, in term of displacement and pore water pressure. The numerical results show relatively good agreement with respect to experiment. It is expected that more accurancy in the prediction could be obtained with a 3D model, in order to reproduce the real boundary conditions of the problem.

We have shown that the hydro-mechanical response of the Opalinus Clay around excavation is governed by four sources of anisotropy: the in-situ stress, the elastic modulus, the plastic

yielding and the water permeability. As a consequence, the global response of Opalinus Clay is quite complex.

In order to reproduce the dependency of the shear strength with the bedding orientation, an extended Drucker-Prager model with an anisotropic cohesion has been developed. The ability of that model to reproduce the behaviour of Opalinus Clay has been proved by numerical simulations of triaxial tests performed with different orientations of loading with respect to bedding plane. Those simulations have been used to calibrate mechanical parameters. The hydraulic parameters have been taken from literature

7. References

Barnichon J.D. (1998). Finite element modelling in structural and petroleum geology. *PhD Thesis, Université de Liège*

Drucker D.C., Prager W. (1952). Solid mechanics and plastic analysis for limit design. *Quarterly of Applied Mathematics, 10(2): 157-165.*

Gens A., Vaunat J., Garitte B., Wileveau Y. (2007). In situ behaviour of a stiff layered clay subject to thermal loading: observations and interpretation. *Geotechnique 57, No. 2, 207–228.*

Graham J., Houlsby G.T. (1982) Anisotropic elasticity of a natural clay. *Géotechnique 33(2), 165-180.*

Laloui, L., François, B. (2008). Benchmark on constitutive modeling of the mechanical behaviour of Opalinus Clay. *Mont Terri Project, Technical Report*

Marschall P., Horseman S. and Gimmi T. (2005). Characterisation of Gas Transport Properties of the Opalinus Clay, a Potential Host Rock Formation for Radioactive Waste Disposal. *Oil & Gas Science and Technology – Rev. IFP, Vol. 60 (2005), No. 1,. 121-139*

Martin, C. D. & Lanyon, G. W. (2003) Measurement of in situ stress in weak rocks at Mont Terri Rock Laboratory, Switzerland. *Int. J. Rock Mech. Mining Sci. 40, Nos 7–8, 1077–1088*.

Trick T., Marschall P., Rösli U., Lettry Y., Bossart P., Enachescu C. (2007). Instrumentation for a gas path through host rock and along sealing experiment. *7th International Symposium on Field Measurements in Geomechanics*

Wileveau, Y. (2005). THM behaviour of host rock (HE-D) experiment: Progress report. *Part 1, Technical Report TR 2005-03. Mont Terri Project.*